

1 **Effects of Mass Ratio Heterogeneity and Coating-Related Optical**
2 **Characteristics on the Light Absorption Enhancement of Black Carbon-**
3 **Containing Particles**

4 **Jing Wei¹, Jin-Mei Ding², Yao Song¹, Xiao-Yuan Wang², Xiang-Yu Pei¹, Sheng-**
5 **Chen Xu², Fei Zhang¹, Zheng-Ning Xu¹, Xu-Dong Tian², Bing-Ye Xu², Zhi-Bin**
6 **Wang^{1,3}**

7 ¹ State Key Laboratory of Soil Pollution Control and Safety, Zhejiang Provincial Key
8 Laboratory of Organic Pollution Process and Control, College of Environmental and
9 Resource Sciences, Zhejiang University, Hangzhou 310058, China

10 ² Ecological and Environmental Monitoring Center of Zhejiang Province, Hangzhou
11 310012, China

12 ³ ZJU-Hangzhou Global Scientific and Technological Innovation Center, Zhejiang
13 University, Hangzhou 311200, China

14 **Correspondence:** Bing-Ye Xu (xubingye@zjemc.org.cn) and Zhi-Bin Wang
15 (wangzhibin@zju.edu.cn)

16

17 **Abstract**

18 Black carbon (BC) is a strong climate forcer, but considerable uncertainty remains in
19 estimating its radiative impact, largely due to persistent gaps between observed and
20 modeled light absorption enhancement (E_{abs}). In this study, we employed a Centrifugal
21 Particle Mass Analyzer and Single Particle Soot Photometer tandem system to
22 characterize mass ratio (M_R , coating-to-BC) of BC-containing particles in Hangzhou,
23 China. Observations across a field campaign revealed low, medium, and high E_{abs}
24 values under varying atmospheric conditions. The uniform core-shell Mie model
25 overestimated E_{abs} , particularly during clean periods (low E_{abs}). To address this, we
26 developed an observationally constrained parameterization for transition-state particles
27 based on M_R -dependent optical transitions behaviors. This approach effectively
28 reconciles modeled and measured E_{abs} across varying pollution conditions. It also
29 emphasizes the importance of incorporating M_R heterogeneity and transition-state
30 optical behavior to improve BC light absorption estimates and reduce uncertainties in
31 assessing radiative effects.

32 **1 Introduction**

33 Black carbon (BC) is a strongly light-absorbing aerosol that effectively absorbs
34 solar radiation, warms the atmosphere, and contributes to direct radiative forcing (DRF)
35 (Bond and Bergstrom, 2006; Seinfeld, 2008). According to IPCC assessments, the
36 global effective DRF of BC ranges from -0.28 to 0.41 W/m^2 (Szopa et al., 2021). To
37 represent the effect of BC particle coatings on absorption, most climate models (Bauer
38 et al., 2013; Chen et al., 2024; Stier et al., 2005; Wang et al., 2023; Zhang et al., 2025b)
39 estimate BC light absorption enhancement (E_{abs}) using Mie theory, defined as the ratio
40 of absorption by coated BC to that of uncoated BC cores, under the assumption of a
41 uniform core-shell structure where BC core is fully encapsulated by coating materials.
42 This approach predicts a monotonic increase in E_{abs} with the coating-to-core mass ratio
43 (M_R), often reaching values up to ~ 2 , consistent with laboratory results (Peng et al.,
44 2016) and the pyroCb smoke (Beeler et al., 2024). However, field observations
45 commonly report lower E_{abs} values, typically around 1.4 and sometimes as low as 1.09
46 (Cappa et al., 2012; Huang et al., 2024), although some studies have found moderate
47 E_{abs} values, with maxima reaching approximately 1.5 (Liu et al., 2015b). This
48 discrepancy mainly stems from the oversimplified assumptions in Mie theory, which
49 fail to capture the real atmospheric complexity in BC size distribution, coating
50 configuration, and mixing state (Wang et al., 2021c). Previous microscopy-based
51 single-particle studied (e.g., TEM and SEM) have visually demonstrated that the
52 ambient BC particles exhibit diverse coating structures and highly heterogeneous
53 mixing states, providing direct evidence of deviation from the idealized core-shell
54 assumption (Adachi et al., 2010; Adachi and Buseck, 2013; China et al., 2013; Wang et
55 al., 2021c). Although microscopy techniques are not employed in this work, these
56 findings highlight the importance of realistically representing BC mixing state and
57 coating characteristics when modeling optical properties. The mismatch between model
58 assumptions and observations has motivated efforts to refine the conceptual modeling
59 approaches for BC aging and coating evolution, which forms the focus of this study.

60 A number of studies have explored the discrepancies in BC E_{abs} from various
61 perspectives. Particle-resolved modeling has demonstrated that both particle-to-particle
62 heterogeneity in M_R and deviations from the idealized core-shell structure can strongly
63 influence absorption estimates (Fierce et al., 2020). In particular, non-uniform or partial
64 coatings at low M_R can lead to the overestimation of E_{abs} by traditional core-shell
65 models. However, these factors alone tend to cannot explain the low E_{abs} frequently
66 observed under high M_R conditions (Huang et al., 2024). Atmospheric BC particles also
67 exhibit substantial variability in their internal mixing state during aging. Fresh BC
68 exhibit a branched structure that collapses into compact shapes with reduced light
69 absorption cross-sections during aging (Moteki and Kondo, 2007; Romshoo et al., 2024;
70 Li et al., 2024; Radney et al., 2014; Corbin et al., 2023). Early aging stage feature
71 uneven coatings, while aged particles show BC core either encapsulated or located near
72 the particle surface (Zhang et al., 2008; Adachi and Buseck, 2013). These aging features
73 are consistent with single-particle observations showing the progressive collapse and
74 coating thickening of BC aggregates during atmospheric processing (Adachi et al., 2016;
75 Ueda et al., 2016), which support the conceptual framework adopted in this study.
76 Recent studies further suggest that the proportion of non-spherical BC particles and the
77 position of the BC core may be key factors contributing to low E_{abs} , leading to an
78 overestimation by core-shell model (Huang et al., 2024; Chen et al., 2024; Zhang et al.,
79 2022). Although this study does not involve direct microscopic measurements or
80 detailed particle-resolved modeling, our work aims to refine the conceptual
81 representation of BC aging and coating evolution to better capture M_R -related optical
82 behavior under ambient conditions.

83 In this study, a suite of state-of-the-art instruments were employed to
84 simultaneously capture the magnitude and temporal of BC M_R in Hangzhou, China
85 (Zhang et al., 2025a; Qian et al., 2025). The ratio of SP2-measured single-particle
86 scattering cross sections to the core-shell Mie theory simulated values was used as an
87 observational proxy to characterize M_R -dependent optical transitions of BC-containing
88 particles (Liu et al., 2017a; Liu et al., 2020). Field measurements revealed the
89 coexistence of high, medium, and low E_{abs} under high bulk-averaged M_R conditions.
90 Based on these observations, the influences of M_R heterogeneity and M_R -dependent
91 optical behavior were quantified to reconcile discrepancies in E_{abs} between model
92 predictions and field observations. Subsequently, an observationally constrained
93 parameterization for “transition-state” BC-containing particles was refined to better
94 reproduce measured E_{abs} under different ambient atmospheric conditions. This study
95 underscores the importance of simultaneously accounting for M_R heterogeneity and M_R -
96 dependent optical transitions when predicting E_{abs} , offering insights that can help reduce
97 uncertainties in estimates of BC direct radiative forcing.

98 **2 Methods**

99 **2.1 Overview of the field campaign and instrumentation**

100 The field measurements were conducted at the Central Air Quality Assurance
101 Monitoring Station (30.25°N, 120.24°E) in Hangzhou from 3th Sept., 2023 to 13th Oct.,

102 2023. The sampling site is located just 100 meters from the Qiantang River in the
103 western part of Hangzhou, with major traffic routes within 3 kilometers to the northeast
104 and southwest of the station. The schematic of the instrumentation is provided in Fig.
105 S1. Aerosols were sampled after passing through a PM_{2.5} impactor and then dried
106 through a diffusion dryer before reaching subsequent instruments.

107 The mass of a BC-containing particle (M_p) and of the BC core (M_{BC_core}) were
108 simultaneously obtained by a Centrifugal Particle Mass Analyzer (CPMA, Cambustion)
109 and a single-particle soot photometer (SP2, DMT Inc.) tandem system. The CPMA
110 classifies particles according to their total mass and has been described in detail by
111 Olfert and Collings (2005). According to the instrument manual, the mass accuracy of
112 the CPMA is approximately 5%. The SP2 measures particle incandescence and
113 scattering to determine BC core mass and optical properties (Stephens et al., 2003;
114 Moteki and Kondo, 2010; Gysel et al., 2011; Schwarz et al., 2022), and the uncertainty
115 associated with the SP2-derived BC core mass (M_{BC_core}) is approximately 10%
116 (Laborde et al., 2012). Previous studies have applied the tandem CPMA-SP2 set up
117 (Cross et al., 2010; Liu et al., 2022; Naseri et al., 2022; Zanatta et al., 2025). In this
118 work, SP2 was calibrated using size-resolved Aquadag aerosols (DMT, 2011) (Fig. S2c
119 and d) following the procedures described by Baumgardner et al. (2012) and Laborde
120 et al. (2012). In this setup, particles with known mass (M_p) selected by CPMA were
121 injected into the SP2. An X-ray aerosol neutralizer (TSI 3088) was installed upstream
122 of the CPMA to charge the aerosols to a Boltzmann equilibrium before entering the
123 classifier.

124 The CPMA was operated over M_p setpoints ranging from 0.9 fg to 30 fg,
125 logarithmically spaced into ten intervals (0.93 fg, 1.37 fg, 2.02 fg, 2.97 fg, 4.36 fg, 6.40
126 fg, 9.39 fg, 13.78 fg, 20.22 fg and 29.68 fg), then the mass of BC core was measured
127 by SP2. The duration of one set point cycle was 1 hour, with each M_p point sampling
128 for 5 minutes, and all M_p points was sampling for total of 50 minutes. The remaining
129 10 minutes were divided into 4 minutes for instrument stabilization and 6 minutes for
130 measuring all BC-containing particles when the valve was switched to the single SP2
131 line. During further data analysis, particles with $M_p = 0.93$ fg and $M_p = 1.37$ fg exhibited
132 excessively noisy scattering signals, likely due to weak signal intensity and low signal-
133 to-noise ratio for small particles, and were therefore excluded from subsequent
134 statistical analysis.

135 In the subsequent data processing, measurements from the CPMA-SP2 system
136 were first corrected for multiple charging effects. Additional corrections, including
137 transfer function, detection efficiency, and time delay, were also applied, as detailed in
138 the Text S1. The mass of each BC core (M_{BC_core}) was then calculated from the SP2
139 incandescence signal using the calibration described above, with a correction factor of
140 0.75 applied to the peak height (Liu et al., 2020; Liu et al., 2014; Zhang et al., 2018;
141 Gysel et al., 2011). The SP2 scattering signal was calibrated with polystyrene latex
142 spheres (PSL) of known sizes (210 nm, 270 nm and 310 nm) (Fig. S2b). Additionally,
143 the calibration of the scattering and the incandescence channels was performed before
144 and after the measurement campaign.

145 The mass concentrations of non-refractive OA, nitrate, sulfate, ammonium and

146 chloride was measured by time-of-flight aerosol chemical speciation monitor with
 147 extended resolution (ToF-ACSM X, Aerodyne). Instrument principles, calibration
 148 procedures, and operational details for the ToF-ACSM X are described in a previous
 149 study of ours (Zhang et al., 2025a). The aerosol extinction and scattering coefficient
 150 (Fig. S3) at wavelength of 440, 530 and 630 nm were measured by Multi-Wavelength
 151 Cavity Attenuated Phase Shift Single-Scattering Albedo Monitor (CAPS-ALB,
 152 Shoreline) (Weber et al., 2022). Absorption was calculated as the difference between
 153 extinction and scattering, with estimated uncertainties of ~1-10% for both extinction
 154 and scattering (Modini et al., 2021), leading to a conservative absorption uncertainty of
 155 ~15-20% for the submicron BC particles considered. No explicit truncation correction
 156 was applied, as the analysis focuses on the relative enhancement of absorption with M_R
 157 rather than absolute values. In this study, only the measurements at 630 nm were used
 158 for subsequent analysis, as this wavelength is minimally affected by brown carbon
 159 absorption. Besides, the aerosol scattering coefficient at wavelength of 450 nm, 525 nm,
 160 and 635 nm was also measured by Multi Wavelength Integrating Nephelometer
 161 (Abbreviation: Nephelometer, Aurora 3000, Acoem) (Schloesser, 2016). The slope of
 162 the scattering coefficient measured by CAPS-ALB and Nephelometer at corresponding
 163 wavelength was close to 1 (Fig. S4), indicating the all data are reliable for further
 164 analysis. Besides, before sampling, the scattering coefficient of CAPS-ALB and
 165 Nephelometer at every wavelength was calibrated using PSL spheres. Monodisperse
 166 PSL particles of different diameters (100 nm, 150 nm, 200 nm and 300 nm) were
 167 selected using a Differential Mobility Analyzer (DMA) and introduced into the
 168 instruments, enabling accurate measurement of their scattering cross section (C_{sca}). The
 169 slope of the C_{sca} measured by CAPS-ALB (or the Nephelometer) and modeled by Mie
 170 theory was close to 1 (Fig. S5), indicating the reliability of the CAPS-ALB and
 171 Nephelometer. The lower detection limit of the Nephelometer at all three wavelengths
 172 was 0.3 Mm^{-1} with a 60-second integration time, while that of the CAPS-ALB was 1
 173 Mm^{-1} with 30-second integration time.

174 **2.2 Mixing state and M_R -dependent optical transitions of the particle-resolved BC-** 175 **containing particles**

176 Under the assumption of singly charged particles, the mixing state of a single BC-
 177 containing particle can be represented by the mass ratio of the BC coating to the BC
 178 core, without relying on assumptions about particle morphology or coating structure,

$$M_R = (M_p - M_{BC_core}) / M_{BC_core} \quad (1)$$

179 where M_p and M_{BC_core} were the total mass and the BC core mass of each BC-containing
 180 particle, respectively. Considering the uncertainties of M_p (5%) and M_{BC_core} (10%), the
 181 uncertainty of M_R for a single BC-containing particle was approximately 11% (Text S2).
 182 Then M_R was converted to the bulk-averaged M_R to be compared with the measured
 183 E_{abs} in bulk particles by summing of total coating and BC core mass of BC-containing
 184 particles each hour,

$$\text{bulk - averaged } M_R = \frac{\sum_i M_{R,i} \times M_{BC_core,i}}{\sum_i M_{BC_core,i}} \quad (2)$$

185 where i was the i^{th} single BC-containing particle. Propagating these uncertainties to the
 186 hourly mass-weighted calculation resulted in an uncertainty of approximately 7% for
 187 the bulk-averaged M_R (Text S2). The data measured by CPMA-SP2 were corrected via
 188 several steps, including (1) correction of delay time, (2) multi-charged particles and (3)
 189 collection efficiency (for details, see Text S1).

190 The M_R -dependent optical transitions of BC-containing particles were further
 191 derived from SP2 measurements at a wavelength of 1064 nm. In the CPMA-SP2 system,
 192 when both M_p and M_{BC_core} are known, the modeled scattering cross section ($C_{sca_modeled}$)
 193 of BC-containing particles can be derived using Mie theory (Wang et al., 2021a). This
 194 calculation assumes a core-shell structure, with the BC core having a refractive index
 195 of 2.26-1.26*i* (Liu et al., 2017a; Zhao et al., 2020) and the non-absorbing coating
 196 characterized by a refractive index of 1.48 and a density of 1.5 g cm⁻³ at a wavelength
 197 of 1064 nm (Liu et al., 2015a). The measured scattering cross section ($C_{sca_measured}$) was
 198 obtained from the SP2 using the leading-edge-only (LEO) technique, which
 199 reconstructs the scattering signal as BC-containing particles pass through the SP2 laser
 200 beam due to partial evaporation of refractory-absorbing material. The validity of this
 201 reconstruction relies on the assumption that the leading-edge data used for fitting
 202 represents an unperturbed particle, as extensively reported in previous studies (Liu et
 203 al., 2014; Zhang et al., 2016; Brooks et al., 2019; Gao et al., 2007; Zhang et al., 2020).
 204 Note only particles with successfully fitted LEO signals are considered in the optical
 205 property calculations. By comparing $C_{sca_measured}$ with $C_{sca_modeled}$, the M_R -dependent
 206 optical behavior of BC-containing particles can be inferred, particularly for transition-
 207 state particles. This comparison captures how variations in coating-to-core mass ratio
 208 influence scattering, providing observational constraints on the optical evolution of BC
 209 during aging (Liu et al., 2017a; Liu et al., 2020). Further methodological details are
 210 provided in Section 3.

211 2.3 The measured and modeled E_{abs}

212 The light absorption enhancement of BC-containing particles is defined as the ratio
 213 of the mass absorption cross section (MAC) of the coated and uncoated BC-containing
 214 particles (Eq. 3). Here, MAC is defined as the particle light absorption cross section
 215 normalized by the BC mass, representing the light absorption per unit mass of BC.

$$E_{abs_measured} = \frac{MAC_{BC_coated_measured}}{MAC_{BC_core_measured}} \quad (3)$$

216 where $E_{abs_measured}$ is the measured light absorption enhancement, and
 217 $MAC_{BC_core_measured}$ is the mass absorption cross section for uncoated BC particles. The
 218 value of $MAC_{BC_core_measured}$ was obtained by extrapolating $MAC_{BC_coated_measured}$ to the
 219 limit of bulk-averaged $M_R = 0$ using linear regression. The $MAC_{BC_core_measured}$ at
 220 wavelength of 630 nm was $9.08 \pm 0.53 \text{ m}^2 \text{ g}^{-1}$ (mean \pm 90% confidence Interval) (Fig.
 221 S6). Based on our error propagation analysis, which accounts for measurement
 222 uncertainties in particle absorption and BC mass as well as the standard error of the
 223 extrapolation, the estimated uncertainty of $MAC_{BC_core_measured}$ is approximately 19-23%
 224 (Text S2). And the uncertainty of $E_{abs_measured}$ is approximately 26 - 32% (Text S2). For
 225 comparison, the $MAC_{BC_core_measured}$ is slightly higher than the value of $7.5 \text{ m}^2 \text{ g}^{-1}$

226 recommended by Bond and Bergstrom (2006) but still within the range reported by
 227 other study ($\sim 6.5 - 17 \text{ m}^2 \text{ g}^{-1}$) (Zanatta et al., 2016), likely due to variations in
 228 measurement methods, and site-specific atmospheric conditions.

229 The commonly used models for calculating the optical properties of BC-
 230 containing particles include Core-shell Mie theory (Cappa et al., 2012), T-matrix (Wu
 231 et al., 2020), and discrete dipole approximation (DDA) (Kahnert and Kanngießer, 2020)
 232 and the generalized Mie Model (Kahnert and Kanngießer, 2020). Among them, T-
 233 matrix, and DDA fully account for detailed particle structure by incorporating three-
 234 dimensional parameters such as particle configuration and internal mixing state (Wu et
 235 al., 2020). In contrast, Core-shell Mie theory relies solely on the BC core size (D_c) and
 236 coating thickness (D_p/D_c). Given the measurement data available in this study, the Core-
 237 shell Mie theory was used to calculate the E_{abs} of BC-containing particles at a
 238 wavelength of 630 nm. The refractive index (RI) of BC and its coatings are assumed to
 239 be $n=1.85+0.71i$ and $n=1.5+0i$ at a wavelength of 630 nm (Liu et al., 2015a; Liu et al.,
 240 2014). The size of BC core and coating thickness was directly measured by CPMA-SP2
 241 tandem system. For the uniform core-shell assumption, the M_R of every D_c was equal
 242 to bulk-averaged M_R (Section 2.2), as described by Cappa et al. (2019) and Liu et al.
 243 (2017a). Then the particle-resolved Core-shell Mie theory was employed to calculate
 244 the MAC_{BC} of individual BC-containing particles. After obtaining the particle-resolved
 245 MAC, we can calculate the MAC of BC particle ensembles as

$$MAC_{BC_coated_modeled} = \frac{\sum_i MAC_{BC_coated_modeled,i} \times M_{BC_core,i}}{\sum_i M_{BC_core,i}} \quad (4)$$

246 where i denotes the i^{th} BC-containing particle, and $MAC_{BC_coated_modeled,i}$ and $M_{BC_core,i}$
 247 represent the particle-resolved modeled MAC of coated BC and the mass of the BC
 248 core, respectively. Then, the modeled E_{abs} of BC particle ensembles are calculated as
 249 the ratio of MAC_{BC_coated} to MAC_{BC_core} . Note that the MAC_{BC_core} here is calculated
 250 using the core-shell Mie model when $D_p/D_c = 1$.

251 To better characterize the influence of coating on the optical response of BC-
 252 containing particles, we derived a parameter based on the ratio between the SP2-
 253 measured scattering cross section ($C_{\text{sca_measured}}$) and the values calculated using the core-
 254 shell Mie model ($C_{\text{sca_modeled}}$) at 1064 nm. This ratio changes consistently with M_R ,
 255 providing an optical indicator of coating-induced variations in particle properties. An
 256 empirical $C_{\text{sca_measured}}-M_R$ relationship (Fig. 3d-f) was then developed using SP2
 257 observations, and subsequently applied to infer the MAC of transition-state BC-
 258 containing particles. The bulk-averaged MAC was obtained by integrating the inferred
 259 MAC over the entire BC population.

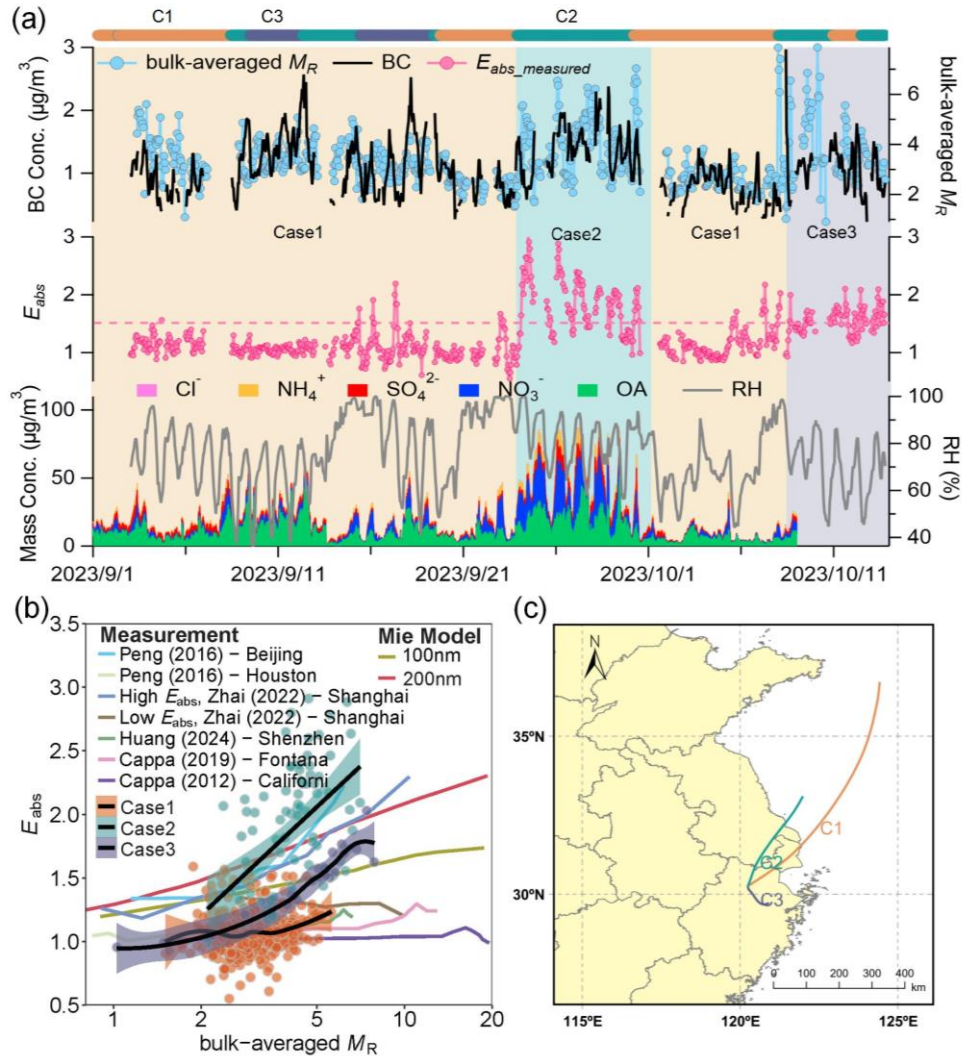
260 **3 Results and discussions**

261 **3.1 Direct observation of different E_{abs} .**

262 The average $E_{\text{abs_measured}}$ during the sampling period in Hangzhou is 1.28 ± 0.02 (mean
 263 $\pm 90\%$ confidence Interval, the same below) at wavelength of 630 nm, and the bulk-
 264 averaged M_R is 3.32 ± 0.06 , with average $E_{\text{abs_measured}}$ values of 1.09 ± 0.02 , 1.84 ± 0.07 ,
 265 and 1.55 ± 0.04 for Case 1, Case 2, and Case 3, respectively. To investigate the temporal

266 evolution of BC coating, the observation period was classified into three cases based
267 on the variation of $E_{\text{abs_measured}}$, using $E_{\text{abs}}=1.5$ as the reference threshold (Fig.1). Case
268 1 (September 3-23 and October 1-7, 2023) corresponds to $E_{\text{abs_measured}}$ significantly
269 below 1.5. These periods were characterized by relatively low non-refractory PM_{10}
270 concentrations and high wind speeds ($\text{WS} = 0.94 \pm 0.04$ m/s). Back-trajectory analysis
271 further shows that Case 1 was dominated by clean marine and nearby local air masses,
272 resulting in relatively clean and weakly aged conditions (Fig. 1a). Case 2 (September
273 24–30) corresponds to periods when $E_{\text{abs_measured}}$ remained continuously higher than 1.5.
274 This episode occurred under stagnant meteorological conditions-characterized by weak
275 winds ($\text{WS} = 0.81 \pm 0.02$ m/s) and elevated relative humidity ($\text{RH} = 81.34 \pm 17.12\%$) -
276 that favored secondary aerosol formation. Back-trajectory analysis further indicates that
277 Case 2 was dominated by air masses transported from Jiangsu and passing through
278 northern Zhejiang, enhancing pollutant accumulation and promoting more aged BC
279 conditions. Case 3 includes periods when $E_{\text{abs_measured}}$ persistently fluctuated around 1.5.
280 The air masses during this period were a mixture of polluted inland outflow and clean
281 marine inflow, suggesting the air masses were moderately aged—which explains the
282 intermediate E_{abs} .

283 Some studies conducted in cities such as Beijing (Peng et al., 2016), Shanghai
284 (Zhai et al., 2022) have observed a notable increase in $E_{\text{abs_measured}}$. In contrast, in cleaner
285 regions like Shenzhen (Huang et al., 2024), Houston (Peng et al., 2016) and California
286 (Cappa et al., 2012; Cappa et al., 2019), even when R_{BC} reached approximately 5,
287 $E_{\text{abs_measured}}$ often showed minimal enhancement. Our observations captured a wide
288 range of $E_{\text{abs_measured}}$ values (0.92~1.84), encompassing high, medium, and low levels.
289 In these three cases, $E_{\text{abs_measured}}$ exhibited distinct evolution patterns during the aging
290 of BC-containing particles (Fig. 1), with its dependence on bulk-averaged M_{R} being
291 minimal in Case 1, moderate in Case 3, and strongest in Case 2. The differences among
292 the three cases may also be associated with variations in meteorological conditions, air
293 mass origin, and chemical composition. On the other hand, in Case 2, the E_{abs} calculated
294 using the traditional core-shell Mie model ($E_{\text{abs_uniform}}$) reasonably agrees with the
295 $E_{\text{abs_measured}}$, whereas Case 3 shows a slightly lower level of consistency. However, in
296 Case 1, the $E_{\text{abs_uniform}}$ predicted by the traditional core-shell Mie model is significantly
297 higher than the $E_{\text{abs_measured}}$. In our subsequent analysis, we will address this discrepancy
298 by exploring both heterogeneity of M_{R} and M_{R} -dependent transitions in optical
299 properties.



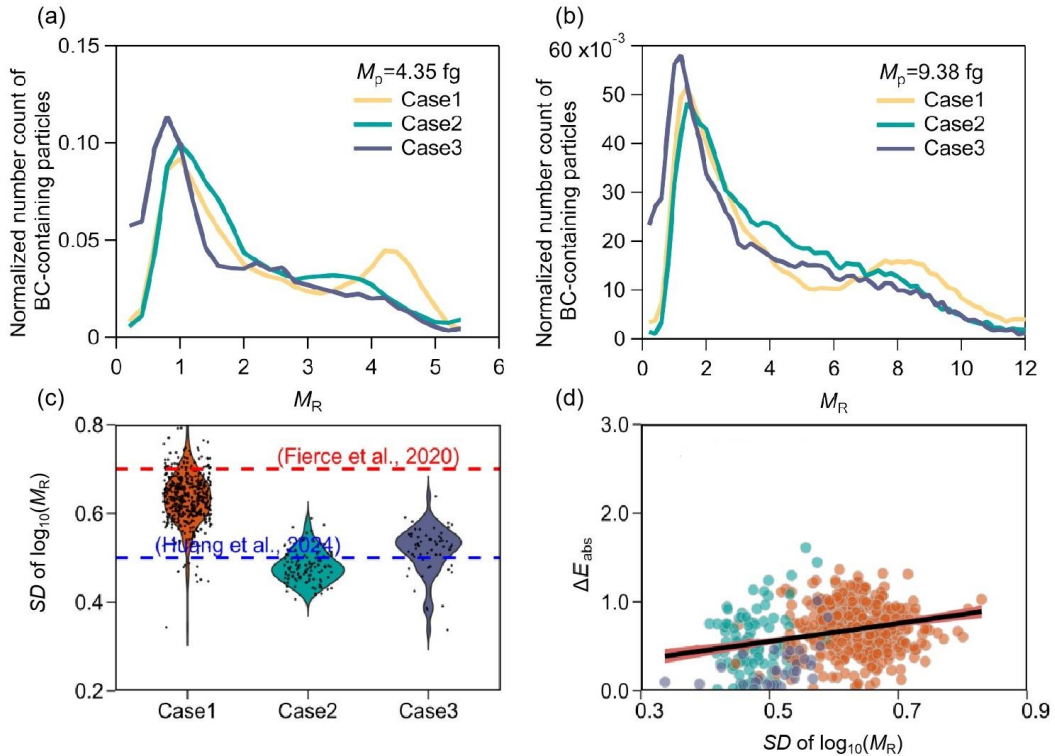
300

301 **Figure. 1** (a) The time series of BC concentrations, bulk-averaged M_R , measured E_{abs} ,
 302 and the chemical components (including organics, nitrate, sulfate, ammonium and
 303 chloride) measured by TOF-ACSM X, as well as relative humidity (RH). Shaded
 304 regions indicate different cases: light yellow for Case 1, blue-green for Case 2, and
 305 gray for Case 3. (b) Comparison of measured E_{abs} in different observation periods and with
 306 previous studies (Peng et al., 2016; Cappa et al., 2012; Zhai et al., 2022; Cappa et al.,
 307 2019; Huang et al., 2024). The black solid line represents the fitted smoothing curve of
 308 bulk-averaged M_R and measured E_{abs} , with the shaded area indicating the 95%
 309 confidence interval of the fit. (c) Mean 48-h back-trajectory simulations initialized at
 310 100 m above ground level. The back trajectories were calculated using the Hybrid
 311 Single-Particle Lagrangian Integrated Trajectory (HYSPLIT) model driven by GDAS
 312 meteorological fields.

313 **3.2 Role of mixing state heterogeneity in E_{abs} and direct evidence of M_R -dependent**
 314 **optical transitions of BC-containing particles.**

315 The coating-to-BC mass ratio (M_R) and the ratio of measured to modeled scattering
 316 cross sections were used to quantify the mixing state and associated optical transitions
 317 behavior of BC-containing particles, with M_R serving as an important indicator of BC

318 aging (Zeng et al., 2024; Li et al., 2024; Liu et al., 2017a). Fig. 2a and 2b illustrated
 319 significant differences in the normalized number distribution of BC-containing particles
 320 at $M_p = 4.35$ fg and 9.38 fg during different observation periods. Specifically, during
 321 Case 2 and Case 3, the M_R presents a unimodal distribution, with the peak value
 322 increasing with increasing M_p . In contrast, during Case 1, the M_R exhibits a distinct
 323 bimodal distribution, and both peak positions shift toward higher M_R values as M_p
 324 increases. For example, when $M_p = 4.35$ fg, the two peaks occur at $M_R = 1$ fg and 4.2
 325 fg, respectively, whereas at $M_p = 9.38$ fg, they shift to $M_R = 1.8$ fg and 8.0 fg,
 326 respectively. The standard deviation (SD) of $\log_{10}(M_R)$ was used to characterize the
 327 heterogeneity of M_R among individual BC-containing at each M_p . The results showed
 328 that the SD of Case 1 (0.63 ± 0.004) was greater than that of Case 3 ($SD = 0.52 \pm 0.012$),
 329 followed by Case 2 ($SD = 0.48 \pm 0.005$). In contrast, the $E_{abs_measured}$ exhibited an
 330 opposite trend, suggesting that greater M_R heterogeneity of BC-containing particles
 331 leads to a lower $E_{abs_measured}$. As shown in Fig. 2d, the discrepancy between the modeled
 332 (uniform core-shell Mie model) and the measured E_{abs} increases with SD , with this trend
 333 being most pronounced in Case 1, where M_R heterogeneity is highest. This suggests that
 334 greater M_R heterogeneity may lead to larger deviations from the uniform core-shell
 335 assumption, thereby increasing the mismatch between the modeled and measured E_{abs} .
 336 Such discrepancies likely due to the uniform core-shell model's simplified treatment of
 337 M_R heterogeneity in BC (Romshoo et al., 2024; Wang et al., 2021c).

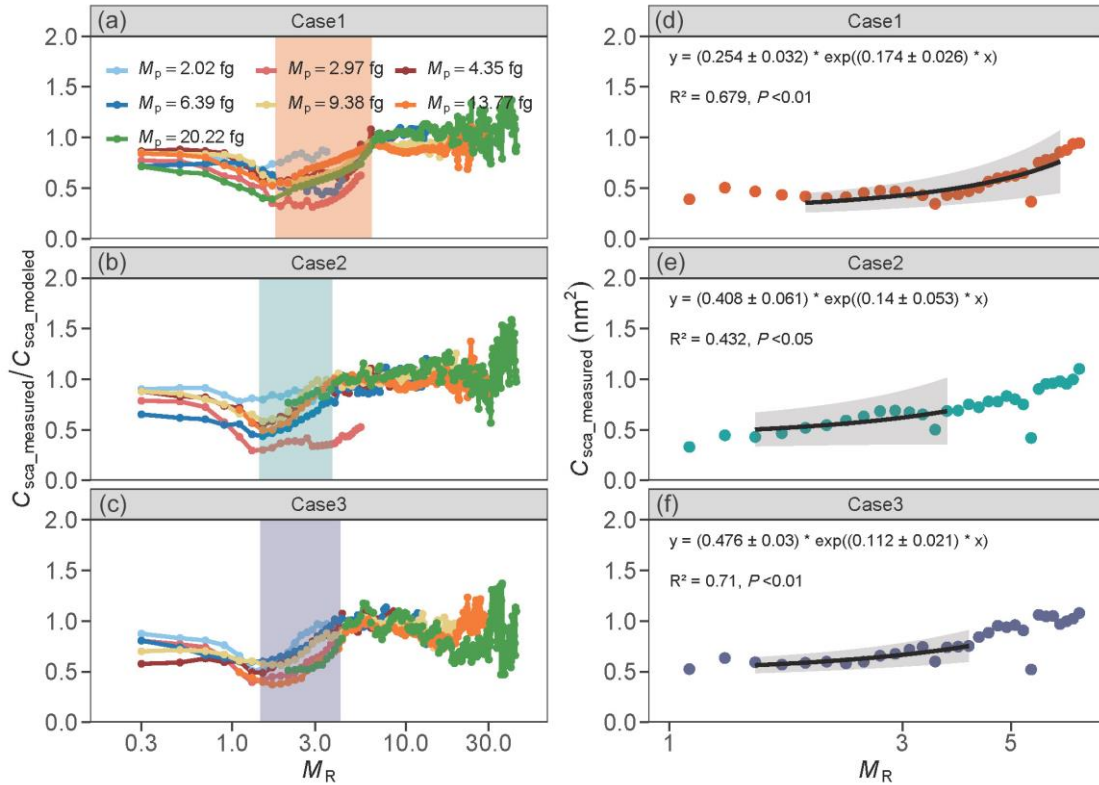


338

339 **Figure. 2** M_R heterogeneity of BC-containing particles in different observation periods.
 340 The average M_R normalized number distribution of BC-containing particles at $M_p =$
 341 4.35 fg (a) and $M_p = 9.38$ fg (b) during different cases. (c) Comparison of the average
 342 standard deviation (SD) of $\log_{10}(M_R)$ in this study with those reported by Huang et al.
 343 (2024) and Fierce et al. (2020), the SD characterizes the dispersion of M_R among

344 individual BC-containing particles. (d) Linear fitting of ΔE_{abs} ($E_{\text{abs_uniform}} - E_{\text{abs_measured}}$)
345 with the SD of $\log_{10}(M_R)$.

346 The SP2 measures the scattering cross-section (C_{sca}) of single BC-containing
347 particles. The comparison between measured and the modeled (by Core-shell Mie
348 model) C_{sca} serves as an optical proxy of changes in BC compaction and coating state,
349 reflecting the evolution of optical properties during aging process. Fig. 3 presents the
350 variation of the ratio $C_{\text{sca_measured}}/C_{\text{sca_modeled}}$ at wavelength of 1064 nm with M_R under
351 different M_p . When M_R is relatively low, $C_{\text{sca_measured}}/C_{\text{sca_modeled}}$ is less than 1, suggesting
352 that the BC cores may exist in a fractal structure, remain bare, or are not fully embedded
353 in the coating materials. Consequently, the measured C_{sca} is lower than the C_{sca}
354 predicted by the core-shell Mie model. This observation aligns with Liu et al. (2017a),
355 who classified such BC-containing particles as externally mixed. As M_R increases,
356 $C_{\text{sca_measured}}/C_{\text{sca_modeled}}$ also increases, indicating the BC particles becomes more
357 compact and more thoroughly coated, transitioning toward a core-shell structure
358 (Corbin et al., 2023). Following previous studies (Liu et al., 2017a; Liu et al., 2020),
359 we describe this stage as a “transition state”. In this work, the transition state is neither
360 defined by a fixed M_R threshold nor by any directly observed morphological boundary.
361 Instead, it reflects an optically inferred state in which scattering enhancement increases
362 markedly, with M_R ranges of 1.78-6.34 (Case 1), 1.43-3.78 (Case 2), and 1.45-4.19
363 (Case 3). The higher M_R thresholds observed in Case 2 and Case 3 indicate that under
364 polluted conditions, BC particles can reach an optically core-shell-like state with
365 comparatively less coating material. This likely reflected accelerated aging driven by
366 enhanced secondary formation and condensation of inorganics and organics on BC,
367 facilitated by stagnant meteorological conditions (low wind speed). Such conditions
368 promote efficient coating growth on BC-containing particles, strengthening their light-
369 absorption capability and leading to high E_{abs} . Therefore, compared with Case 1, BC in
370 Case 2 and Case 3 required less coating material to reach the core-shell configuration.
371 When M_R exceeds the transition state range, the ratio $C_{\text{sca_measured}}/C_{\text{sca_modeled}}$ becomes
372 relatively stable, suggesting that the BC particles behave optically like compact,
373 spherical core-shell structures.



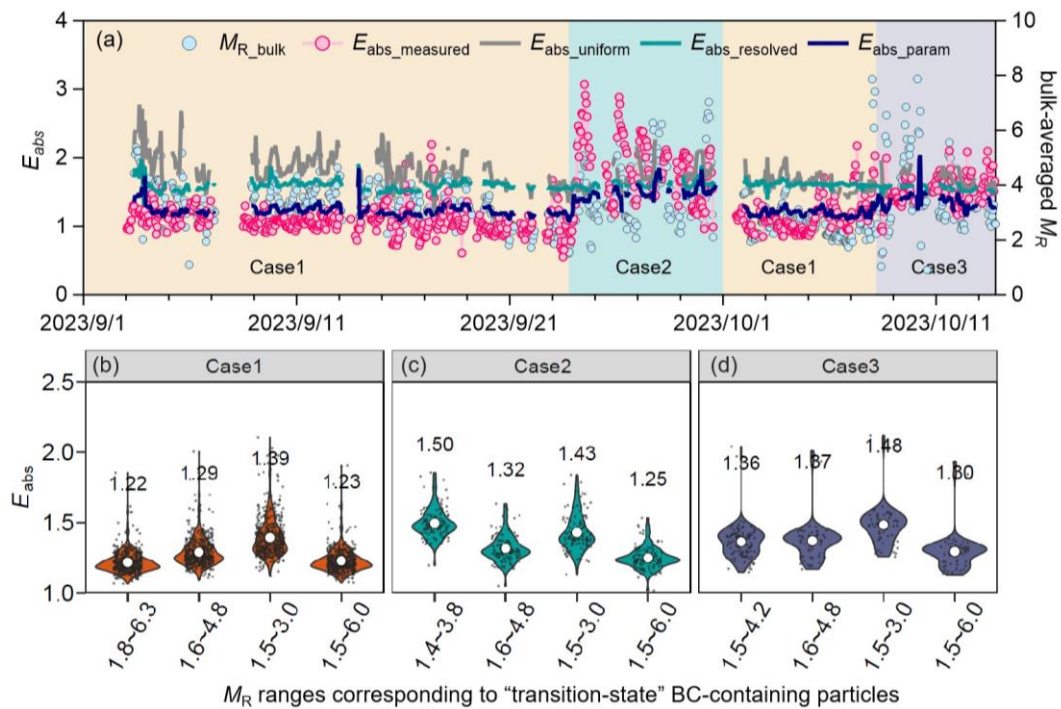
374

375 **Figure. 3** The optical behavior of BC-containing particles as a function of mass ratio
 376 (coating-to-BC, M_R). (a) – (c) show the ratio of measured to modeled scattering cross-
 377 section at the wavelength of 1064 nm during different cases. The shadows indicate the
 378 M_R ranges corresponding to “transition-state” BC-containing particles. (d) – (f) present
 379 the measured scattering cross-section as a function of M_R , along with fitted optical
 380 transition-dependent models representing the “transition-state” BC-containing particles.
 381 The fitted curves include the corresponding P-values, and the shaded areas denote the
 382 95% confidence intervals.

383 3.3 The predicted E_{abs} during different period.

384 The complexity of BC in the atmosphere depends on various factors, including the
 385 size, the coating amount, and the interaction between the BC core and its coating. In
 386 this study, comprehensive multidimensional information on single BC-containing
 387 particle is retrieved and subsequently incorporated into the optical model, as shown in
 388 Fig. 4. The bias between $E_{abs_uniform}$ and $E_{abs_measured}$ varies across different periods, even
 389 when applying the same model input scheme. Specially, the $E_{abs_uniform}$ agrees with
 390 $E_{abs_measured}$ during Case 2 and Case 3, with deviations below 10%, whereas the
 391 deviation increases to as much as to 65% during Case 1, primarily due to the higher M_R
 392 dispersion of BC-containing particles in this period. To further investigate this
 393 discrepancy, we assume that all BC-containing particles adopt a core-shell structure and
 394 calculate the E_{abs} of each BC-containing particle based on the measured single-particle
 395 M_R . Subsequently, the E_{abs} of bulk BC-containing particles ($E_{abs_resolved}$) was determined
 396 and compared with $E_{abs_measured}$ to evaluate their consistency. The results show that for
 397 Case 1, although the discrepancy between the measured and modeled values exhibits a

398 decreasing trend, the average deviation remains as high as 38%. This larger deviation,
 399 compared to previous particle-resolved modeling studies, is primarily attributed to the
 400 smaller dispersion of particle-to-particle M_R observed in Case 1 (Fig. 2c) relative to
 401 their model simulations (Fierce et al., 2020). However, for Case 2 and Case 3 with
 402 higher M_R heterogeneity of BC-containing particles, the error between the model and
 403 measured E_{abs} is almost negligible, with deviations below 10%, indicating that the core-
 404 shell Mie model can reproduce the observed E_{abs} during these periods. These findings
 405 further validate that the degree of M_R dispersion of BC-containing particles is a key
 406 factor in determining whether the core-shell Mie model overestimates the observed E_{abs} ,
 407 and to what extent this overestimation occurs.



408
 409 **Figure. 4** Comparison of measured and modeled E_{abs} under various different model
 410 input schemes. (a) shows the time series of the E_{abs} during the observation period. (b)
 411 – (d) were the sensitivity of E_{abs} to the “transition state” range of BC-containing
 412 particles. The “transition state” range of 1.6~4.8 was the average value derived from
 413 Case 1, Case 2 and Case 3. The range of 1.5~3.0 and 1.5~6.0 was reported by Liu et al.
 414 (2017a), and Liu et al. (2020), respectively.

415 The transitional-state particles are BC-containing particles in the process of
 416 evolving from loosely aggregated fractal-like structures toward quasi-core-shell
 417 configurations (Moffet et al., 2016; Moteki and Kondo, 2007). The abundance of
 418 transitional-state particles varies notably under different atmospheric conditions,
 419 directly influencing the measured E_{abs} (Liu et al., 2017a). During clean days (Case 1),
 420 the atmospheric environment was characterized by low PM_{10} concentrations, weak
 421 secondary formation, and highly variable coating conditions. Under such conditions,
 422 our measurements show that BC-containing particles were dominated by transitional-
 423 state structures (Fig. S9), representing the intermediate stage between externally mixed
 424 aggregates and fully developed quasi-core-shell structures. The limited and

425 heterogeneous coating distribution on these particles substantially weakens the lensing
426 effect, resulting in lower measured E_{abs} (Peng et al., 2016). Because the core-shell Mie
427 model inherently assumes a uniform and concentric coating, it does not accurately
428 represent the optical behavior of these transitional particles, leading to a pronounced
429 overestimation of measured E_{abs} during Case 1. This indicates that, under clean
430 conditions, the optical properties of transitional-state particles are the key driver of the
431 model-observation discrepancy. In contrast, the haze period (Case 2) represents a more
432 aged and heavily coated aerosol environment and provides a useful reference for
433 understanding the factors influencing the measured E_{abs} . During Case 2, the high aerosol
434 loading and elevated bulk-averaged M_R were largely influenced by regional transport,
435 as air masses at 100 m, 500 m, and 1000 m all followed similar pathways from the
436 northern Yangtze River Delta into northern Zhejiang (Fig. 1c and Fig. S7). Stagnant
437 meteorological conditions, elevated relative humidity, and enhanced oxidative capacity
438 further facilitated vigorous liquid-phase and photochemical reactions, promoting the
439 abundant formation of secondary coatings on BC surfaces (Peng et al., 2016). Notably,
440 our observations show that E_{abs} increases systematically with the increasing
441 contribution of secondary nitrate (Fig. S8), consistent with the fact that nitrate-rich
442 conditions enhance aqueous-phase oxidation and accelerate the formation of thick
443 inorganic coatings (Liu et al., 2017b). As a result, a much larger fraction of BC-
444 containing particles exhibited internally mixed, quasi-core-shell structures rather than
445 transitional states (Fig. S9), which explains why the core-shell Mie model performs
446 substantially better for Case 2 than for Case 1. This contrast reinforces the central role
447 of transitional-state particles in determining measured E_{abs} when coatings are sparse,
448 irregular, or partially developed. Given the strong influence of transitional-state
449 particles on measured E_{abs} in Case 1, precise constraints on their optical behavior are
450 crucial for improving E_{abs} estimates across different atmospheric scenarios. To address
451 this, an empirical formula based on optical measurements was developed to estimate
452 the E_{abs} of BC-containing particles in the “transition state”, derived from fitting the
453 measured C_{sca} against M_R (Fig. 3d-3f). By applying this empirical formula to the
454 calculation of E_{abs} , the resulting value for Case 1 was 1.21 ± 0.01 . For Case 2 and Case
455 3, the E_{abs} calculated using the same formula ($E_{\text{abs_param}}$) remained slightly lower than
456 the $E_{\text{abs_measured}}$, but the deviation was within 20%, demonstrating the reliability of the
457 approach across different atmospheric conditions.

458 In recent years, particle-resolved models have been increasingly applied in field
459 observations to mitigate the well-known overestimation of E_{abs} by uniform core-shell
460 Mie model (Fierce et al., 2020; Li et al., 2024; Jiang et al., 2025). Some studies have
461 incorporated particle-specific structural detail using approaches such as the electron-
462 microscope-to-BC-simulation (EMBS) framework (Wang et al., 2021c; Wang et al.,
463 2021b; Chakrabarty et al., 2006), which further improves the representation of BC
464 absorption. In this study, we introduce an observationally constrained parameterization
465 that links SP2-measured scattering cross sections with core-shell Mie calculations. This
466 scheme identifies the optical transition state through following steps: (1) measuring
467 single-particle C_{sca} with SP2, (2) fitting the relationship between $C_{\text{sca_measured}}$ and M_R
468 (Fig. 4b-4c), (3) identifying the M_R range associated with transitional optical behavior

469 (“transition state”), and (4) inferring the MAC of transition-state particles using the
470 fitted relationship before integrating MAC over all particles to obtain bulk E_{abs} . This
471 parameterization improves agreement with observations, especially during clean
472 periods (Case 1), when the uniform core-shell assumption tends to produce the largest
473 discrepancies. However, its performance depends on correctly identifying the M_{R} range
474 of the transition state. Our results show that, in polluted periods (Cases 2 and 3), the M_{R}
475 range associated with the transition-state becomes relatively narrow, while under clean
476 conditions it tends to expand. Consequently, applying a fixed M_{R} threshold across all
477 atmospheric conditions can introduce systematic biases in modeled E_{abs} (Fig. 4b, c and
478 d). Although M_{R} heterogeneity alone can adequately reproduce E_{abs} during polluted
479 periods, adopting separate input schemes for different environments would complicate
480 radiative transfer calculations and limit broader applicability.

481 To address this issue, we emphasize that the proposed framework is adaptable to
482 environments in which BC particles undergo similar optical transitions. Key parameters,
483 including the M_{R} thresholds that define the transition state and other indicators derived
484 from the $C_{\text{sca_measured}}-M_{\text{R}}$ relationship, can be recalibrated for different atmospheric
485 contexts. This includes rural areas, biomass-burning regions, or seasons with distinct
486 pollution characteristics, where coating composition and aging processes may vary.
487 Although the parameterization is fundamentally based on the optical evolution of BC
488 from loosely coated to more compact states, it can be adjusted to account for local
489 differences in particle coating and aging dynamics. Thus, the unified scheme
490 incorporates both M_{R} variability and optical characteristics of transitional particles,
491 providing a flexible and physically consistent approach for a wide range of atmospheric
492 environments. Overall, this observationally constrained approach offers a more
493 consistent representation of BC mixing states across diverse atmospheric conditions,
494 thereby reducing uncertainties in optical modeling and enhancing the reliability of BC
495 radiative effect assessments.

496 **4 Conclusions**

497 In this study, we employed the CPMA-SP2 tandem system to investigate the mass
498 ratio of coating to core (M_{R}) of BC-containing particles in Hangzhou, China, and to
499 assess how M_{R} heterogeneity and optical transitions influence their E_{abs} under different
500 atmospheric conditions. By dividing the observation into three representative scenarios
501 (Case 1, Case 2, and Case 3), we identified significant differences in the measured E_{abs}
502 that are closely associated with the evolution and distribution of M_{R} . The results indicate
503 that both M_{R} heterogeneity and optical effects of BC-containing particles in the
504 transition state are critical for accurately modeling BC E_{abs} . During clean periods (Case
505 1), the uniform core-shell Mie model significantly overestimated E_{abs} , while during
506 polluted periods (Case 2 and Case 3), model predictions were more consistent with the
507 measured E_{abs} . To address these discrepancies, we developed an observationally
508 constrained parameterization for BC particles in the transition state based on the
509 transitional optical behavior. This scheme effectively reconciles modeled and measured
510 E_{abs} across different pollution scenarios, particularly in clean periods dominated by
511 externally mixed or partially coated BC-containing particles. These results highlight the

512 limitations of uniform model input schemes under complex atmospheric conditions and
513 underscore the value of a unified parameterization framework that accounts for both
514 M_R heterogeneity and the optical properties of transition-state particles. By
515 incorporating M_R -dependent optical transitions, this framework provides an adaptable
516 approach for representing BC mixing states and light absorption under different
517 atmospheric environments. This parameterization improves the consistency between
518 modeled and observed E_{abs} and reduces uncertainties in assessing the radiative effects
519 of BC-containing particles, offering a flexible tool for application to other atmospheric
520 conditions.

521 **Data availability.** The data are available from the link:
522 <http://doi.org/10.6084/m9.figshare.29097263>.

523 **Author contributions.**

524 Conceptualization: Jing Wei, Zhi-Bin Wang

525 Data curation: Jing Wei, Yao Song, Xiang-Yu Pei, Fei Zhang, Zheng-Ning Xu, Jin-Mei
526 Ding, Xiao-Yuan Wang, Sheng-Chen Xu, Xu-Dong Tian, Bing-Ye Xu

527 Formal analysis: Jing Wei

528 Funding acquisition: Zhi-Bin Wang, Bing-Ye Xu

529 Investigation: Zhi-Bin Wang

530 Methodology: Jing Wei, Zhi-Bin Wang

531 Visualization: Jing Wei, Zhi-Bin Wang

532 Writing – original draft: Jing Wei

533 **Competing interests.** At least one of the (co-)authors is a member of the editorial board
534 of *Atmospheric Chemistry and Physics*.

535

536 **Financial support.** This research was supported by the Joint Fund of Zhejiang
537 Provincial Natural Science Foundation of China (LZJMZ25D050003), the National
538 Key Research and Development Program of China (2022YFC3703505), the National
539 Natural Science Foundation of China (42305098), the China Postdoctoral Science
540 Foundation (2023M733028), the Key Laboratory of Formation and Prevention of
541 Urban Air Pollution Complex, Ministry of Ecology and Environment (2025080166).

542 **References**

543 Adachi, K. and Buseck, P. R.: Changes of ns-soot mixing states and shapes in an urban area during
544 CalNex, *Journal of Geophysical Research-Atmospheres*, 118, 3723-3730, 10.1002/jgrd.50321,
545 2013.

546 Adachi, K., Chung, S. H., and Buseck, P. R.: Shapes of soot aerosol particles and implications for their
547 effects on climate, *Journal of Geophysical Research: Atmospheres*, 115, D15206,
548 10.1029/2009jd012868, 2010.

549 Adachi, K., Moteki, N., Kondo, Y., and Igarashi, Y.: Mixing states of light-absorbing particles measured
550 using a transmission electron microscope and a single-particle soot photometer in Tokyo, Japan,

551 Journal of Geophysical Research-Atmospheres, 121, 9153-9164, 10.1002/2016jd025153, 2016.

552 Bauer, S. E., Ault, A. P., and Prather, K. A.: Evaluation of aerosol mixing state classes in the GISS
553 modelE-MATRIX climate model using single-particle mass spectrometry measurements, Journal of
554 Geophysical Research: Atmospheres, 118, 9834-9844, 10.1002/jgrd.50700, 2013.

555 Baumgardner, D., Popovicheva, O., Allan, J., Bernardoni, V., Cao, J., Cavalli, F., Cozic, J., Diapouli, E.,
556 Eleftheriadis, K., Genberg, P. J., Gonzalez, C., Gysel, M., John, A., Kirchstetter, T. W., Kuhlbusch,
557 T. A. J., Laborde, M., Lack, D., Müller, T., Niessner, R., Petzold, A., Piazzalunga, A., Putaud, J. P.,
558 Schwarz, J., Sheridan, P., Subramanian, R., Swietlicki, E., Valli, G., Vecchi, R., and Viana, M.: Soot
559 reference materials for instrument calibration and intercomparisons: a workshop summary with
560 recommendations, Atmospheric Measurement Techniques, 5, 1869-1887, 10.5194/amt-5-1869-
561 2012, 2012.

562 Beeler, P., Kumar, J., Schwarz, J. P., Adachi, K., Fierce, L., Perring, A. E., Katich, J. M., and Chakrabarty,
563 R. K.: Light absorption enhancement of black carbon in a pyrocumulonimbus cloud, Nature
564 Communications, 15, 10.1038/s41467-024-50070-0, 2024.

565 Bond, T. C. and Bergstrom, R. W.: Light Absorption by Carbonaceous Particles: An Investigative Review,
566 Aerosol Science and Technology, 40, 27-67, 10.1080/02786820500421521, 2006.

567 Brooks, J., Liu, D., Allan, J. D., Williams, P. I., Haywood, J., Highwood, E. J., Kompalli, S. K., Babu, S.
568 S., Satheesh, S. K., Turner, A. G., and Coe, H.: Black carbon physical and optical properties across
569 northern India during pre-monsoon and monsoon seasons, Atmospheric Chemistry and Physics, 19,
570 13079-13096, 10.5194/acp-19-13079-2019., 2019.

571 Cappa, C. D., Zhang, X., Russell, L. M., Collier, S., Lee, A. K. Y., Chen, C. L., Betha, R., Chen, S., Liu,
572 J., Price, D. J., Sanchez, K. J., McMeeking, G. R., Williams, L. R., Onasch, T. B., Worsnop, D. R.,
573 Abbatt, J., and Zhang, Q.: Light Absorption by Ambient Black and Brown Carbon and its
574 Dependence on Black Carbon Coating State for Two California, USA, Cities in Winter and Summer,
575 Journal of Geophysical Research: Atmospheres, 124, 1550-1577, 10.1029/2018JD029501, 2019.

576 Cappa, C. D., Onasch, T. B., Massoli, P., Worsnop, D. R., Bates, T. S., Cross, E. S., Davidovits, P., Hakala,
577 J., Hayden, K. L., Jobson, B. T., Kolesar, K. R., Lack, D. A., Lerner, B. M., Li, S.-M., Mellon, D.,
578 Nuaaman, I., Olfert, J. S., Petäjä, T., Quinn, P. K., Song, C., Subramanian, R., Williams, E. J., and
579 Zaveri, R. A.: Radiative Absorption Enhancements Due to the Mixing State of Atmospheric Black
580 Carbon, Science, 337, 1078-1081, <https://doi.org/10.1126/science.1223447>, 2012.

581 Chakrabarty, R. K., Moosmueller, H., Arnott, W. P., Garro, M. A., and Walker, J.: Structural and fractal
582 properties of particles emitted from spark ignition engines, Environmental Science & Technology,
583 40, 6647-6654, 10.1021/es060537y, 2006.

584 Chen, G., Liu, C., Wang, J., Yin, Y., and Wang, Y.: Accounting for Black Carbon Mixing State,
585 Nonsphericity, and Heterogeneity Effects in Its Optical Property Parameterization in a Climate
586 Model, Journal of Geophysical Research: Atmospheres, 129, e2024JD041135,
587 10.1029/2024JD041135, 2024.

588 China, S., Mazzoleni, C., Gorkowski, K., Aiken, A. C., Dubey, M. K., and Michigan Technological Univ,
589 H. M. I.: Morphology and mixing state of individual freshly emitted wildfire carbonaceous particles,
590 Nature Communications, 4, 2122-2122, 10.1038/ncomms3122, 2013.

591 Corbin, J. C., Modini, R. L., and Gysel-Beer, M.: Mechanisms of soot-aggregate restructuring and
592 compaction, Aerosol Science and Technology, 57, 89-111, 10.1080/02786826.2022.2137385, 2023.

593 Cross, E. S., Onasch, T. B., Ahern, A., Wrobel, W., Slowik, J. G., Olfert, J., Lack, D. A., Massoli, P.,
594 Cappa, C. D., Schwarz, J. P., Spackman, J. R., Fahey, D. W., Sedlacek, A., Trimborn, A., Jayne, J.

595 T., Freedman, A., Williams, L. R., Ng, N. L., Mazzoleni, C., Dubey, M., Brem, B., Kok, G.,
596 Subramanian, R., Freitag, S., Clarke, A., Thornhill, D., Marr, L. C., Kolb, C. E., Worsnop, D. R.,
597 and Davidovits, P.: Soot Particle Studies Instrument Inter-Comparison Project Overview, *Aerosol*
598 *Science and Technology*, 44, 592-611, 10.1080/02786826.2010.482113, 2010.

599 Fierce, L., Onasch, T. B., Cappa, C. D., Mazzoleni, C., China, S., Bhandari, J., Davidovits, P., Al Fischer,
600 D., Helgestad, T., Lambe, A. T., Sedlacek, A. J., Smith, G. D., Wolff, L., Brookhaven National Lab,
601 U. N. Y., and Pacific Northwest National Lab, R. W. A.: Radiative absorption enhancements by
602 black carbon controlled by particle-to-particle heterogeneity in composition, *Proceedings of the*
603 *National Academy of Sciences*, 117, 5196-5203, 10.1073/pnas.1919723117, 2020.

604 Gao, R. S., Schwarz, J. P., Kelly, K. K., Fahey, D. W., Watts, L. A., Thompson, T. L., Spackman, J. R.,
605 Slowik, J. G., Cross, E. S., Han, J. H., Davidovits, P., Onasch, T. B., and Worsnop, D. R.: A Novel
606 Method for Estimating Light-Scattering Properties of Soot Aerosols Using a Modified Single-
607 Particle Soot Photometer, *Aerosol Science and Technology*, 41, 125-135,
608 10.1080/02786820601118398, 2007.

609 Gysel, M., Laborde, M., Olfert, J. S., Subramanian, R., and Gröhn, A. J.: Effective density of Aquadag
610 and fullerene soot black carbon reference materials used for SP2 calibration, *Atmospheric*
611 *Measurement Techniques*, 4, 2851-2858, 10.5194/amt-4-2851-2011, 2011.

612 Huang, X.-F., Peng, Y., Wei, J., Peng, J., Lin, X.-Y., Tang, M.-X., Cheng, Y., Men, Z., Fang, T., Zhang,
613 J., He, L.-Y., Cao, L. M., Liu, C., Zhang, C., Mao, H., Seinfeld, J. H., and Wang, Y.: Microphysical
614 complexity of black carbon particles restricts their warming potential, *One Earth*, 7,
615 10.1016/j.oneear.2023.12.004, 2024.

616 Jiang, F., Zheng, Z., Coe, H., Healy, R. M., Poulain, L., Gros, V., Zhang, H., Li, W., Liu, D., West, M.,
617 Topping, D., and Riemer, N.: Integrating Simulations and Observations: A Foundation Model for
618 Estimating the Aerosol Mixing State Index, *Environmental Science & Technology Air*,
619 10.1021/acsestair.4c00329, 2025.

620 Kahnert, M. and Kanngießer, F.: Modelling optical properties of atmospheric black carbon aerosols,
621 *Journal of Quantitative Spectroscopy & Radiative Transfer*, 244, 106849,
622 10.1016/j.jqsrt.2020.106849, 2020.

623 Laborde, M., Schnaiter, M., Linke, C., Saathoff, H., Naumann, K. H., Möhler, O., Berlenz, S., Wagner,
624 U., Taylor, J. W., Liu, D., Flynn, M., Allan, J. D., Coe, H., Heimerl, K., Dahlkötter, F., Weinzierl,
625 B., Wollny, A. G., Zanatta, M., Cozic, J., Laj, P., Hitzenberger, R., Schwarz, J. P., and Gysel, M.:
626 Single Particle Soot Photometer intercomparison at the AIDA chamber, *Atmospheric Measurement*
627 *Techniques*, 5, 3077-3097, 10.5194/amt-5-3077-2012, 2012.

628 Li, W., Riemer, N., Xu, L., Wang, Y., Adachi, K., Shi, Z., Zhang, D., Zheng, Z., and Laskin, A.:
629 Microphysical properties of atmospheric soot and organic particles: measurements, modeling, and
630 impacts, *npj Climate and Atmospheric Science*, 7, 65, 10.1038/s41612-024-00610-8, 2024.

631 Liu, D., Taylor, J. W., Young, D. E., Flynn, M. J., Coe, H., and Allan, J. D.: The effect of complex black
632 carbon microphysics on the determination of the optical properties of brown carbon: BC
633 morphology on BrC optical properties, *Geophysical Research Letters*, 42, 613-619,
634 10.1002/2014GL062443, 2015a.

635 Liu, D., Allan, J. D., Young, D. E., Coe, H., Beddows, D., Fleming, Z. L., Flynn, M. J., Gallagher, M. W.,
636 Harrison, R. M., Lee, J., Prevot, A. S. H., Taylor, J. W., Yin, J., Williams, P. I., and Zotter, P.: Size
637 distribution, mixing state and source apportionment of black carbon aerosol in London during
638 wintertime, *Atmospheric Chemistry and Physics*, 14, 10061-10084, 10.5194/acp-14-10061-2014,

639 2014.

640 Liu, D., Whitehead, J., Alfarra, M. R., Reyes-Villegas, E., Spracklen, D. V., Reddington, C. L., Kong, S.,
641 Williams, P. I., Ting, Y.-C., Haslett, S., Taylor, J. W., Flynn, M. J., Morgan, W. T., McFiggans, G.,
642 Coe, H., and Allan, J. D.: Black-carbon absorption enhancement in the atmosphere determined by
643 particle mixing state, *Nature Geoscience*, 10, 184-188, 10.1038/ngeo2901, 2017a.

644 Liu, H., Pan, X., Liu, D., Liu, X., Chen, X., Tian, Y., Sun, Y., Fu, P., and Wang, Z.: Mixing characteristics
645 of refractory black carbon aerosols at an urban site in Beijing, *Atmospheric Chemistry and Physics*,
646 20, 5771-5785, 10.5194/acp-20-5771-2020, 2020.

647 Liu, H., Pan, X. L., Wang, D. W., Liu, X. Y., Tian, Y., Yao, W. J., Lei, S. D., Zhang, Y. T., Li, J., Lei, L.,
648 Xie, C. H., Fu, P. Q., Sun, Y. L., and Wang, Z. F.: Mixing characteristics of black carbon aerosols in
649 a coastal city using the CPMA-SP2 system, *Atmospheric Research*, 265,
650 10.1016/j.atmosres.2021.105867, 2022.

651 Liu, S., Aiken, A. C., Gorkowski, K., Dubey, M. K., Cappa, C. D., Williams, L. R., Herndon, S. C.,
652 Massoli, P., Fortner, E. C., Chhabra, P. S., Brooks, W. A., Onasch, T. B., Jayne, J. T., Worsnop, D.
653 R., China, S., Sharma, N., Mazzoleni, C., Xu, L., Ng, N. L., Liu, D., Allan, J. D., Lee, J. D., Fleming,
654 Z. L., Mohr, C., Zotter, P., Szidat, S., Prévôt, A. S. H., Los Alamos National Lab, L. A. N. M., and
655 Univ. of California, D. C. A.: Enhanced light absorption by mixed source black and brown carbon
656 particles in UK winter, *Nature Communications*, 6, 8435-8435, 10.1038/ncomms9435, 2015b.

657 Liu, Y., Wu, Z., Wang, Y., Xiao, Y., Gu, F., Zheng, J., Tan, T., Shang, D., Wu, Y., Zeng, L., Hu, M.,
658 Bateman, A. P., and Martin, S. T.: Submicrometer Particles Are in the Liquid State during Heavy
659 Haze Episodes in the Urban Atmosphere of Beijing, China, *Environmental Science & Technology*
660 *Letters*, 4, 427-432, 10.1021/acs.estlett.7b00352, 2017b.

661 Modini, R. L., Corbin, J. C., Brem, B. T., Irwin, M., Bertò, M., Pileci, R. E., Fetfatzis, P., Eleftheriadis,
662 K., Henzing, B., Moerman, M. M., Liu, F., Müller, T., and Gysel-Beer, M.: Detailed characterization
663 of the CAPS single-scattering albedo monitor (CAPS PMssa) as a field-deployable instrument for
664 measuring aerosol light absorption with the extinction-minus-scattering method, *Atmos. Meas.*
665 *Tech.*, 14, 819-851, 10.5194/amt-14-819-2021, 2021.

666 Moffet, R. C., O'Brien, R. E., Alpert, P. A., Kelly, S. T., Pham, D. Q., Gilles, M. K., Knopf, D. A., Laskin,
667 A., Pacific Northwest National Lab, R. W. A. E. M. S. L., Lawrence Berkeley National Lab, B. C.
668 A., and Stony Brook Univ, S. B. N. Y.: Morphology and mixing of black carbon particles collected
669 in central California during the CARES field study, *Atmospheric chemistry and physics*, 16, 14515-
670 14525, 10.5194/acp-16-14515-2016, 2016.

671 Moteki, N. and Kondo, Y.: Effects of Mixing State on Black Carbon Measurements by Laser-Induced
672 Incandescence, *Aerosol Science and Technology*, 41, 398-417, 10.1080/02786820701199728, 2007.

673 Moteki, N. and Kondo, Y.: Dependence of Laser-Induced Incandescence on Physical Properties of Black
674 Carbon Aerosols: Measurements and Theoretical Interpretation, *Aerosol Science and Technology*,
675 44, 663-675, 10.1080/02786826.2010.484450, 2010.

676 Naseri, A., Sipkens, T. A., Rogak, S. N., and Olfert, J. S.: Optimized instrument configurations for tandem
677 particle mass analyzer and single particle-soot photometer experiments, *Journal of Aerosol Science*,
678 160, 10.1016/j.jaerosci.2021.105897, 2022.

679 Olfert, J. S. and Collings, N.: New method for particle mass classification - the Couette centrifugal
680 particle mass analyzer, *Journal of Aerosol Science*, 36, 1338-1352, 10.1016/j.jaerosci.2005.03.006,
681 2005.

682 Peng, J., Hu, M., Guo, S., Du, Z., Zheng, J., Shang, D., Zamora, M. L., Zeng, L., Shao, M., Wu, Y.-S.,

683 Zheng, J., Wang, Y., Glen, C. R., Collins, D. R., Molina, M. J., and Zhang, R.: Markedly enhanced
684 absorption and direct radiative forcing of black carbon under polluted urban environments,
685 Proceedings of the National Academy of Sciences, 113, 4266-4271, 10.1073/pnas.1602310113,
686 2016.

687 Qian, H., Xu, B., Xu, Z., Zou, Q., Zi, Q., Zuo, H., Zhang, F., Wei, J., Pei, X., Zhou, W., Jin, L., Tian, X.,
688 Zhao, W., and Wang, Z.: Anthropogenic Oxygenated Volatile Organic Compounds Dominate
689 Atmospheric Oxidation Capacity and Ozone Production via Secondary Formation of Formaldehyde
690 in the Urban Atmosphere, ACS ES&T Air, 2, 1033-1041, 10.1021/acsestair.4c00317, 2025.

691 Radney, J. G., You, R. A., Ma, X. F., Conny, J. M., Zachariah, M. R., Hodges, J. T., and Zangmeister, C.
692 D.: Dependence of Soot Optical Properties on Particle Morphology: Measurements and Model
693 Comparisons, Environmental Science & Technology, 48, 3169-3176, 10.1021/es4041804, 2014.

694 Romshoo, B., Müller, T., Ahlawat, A., Wiedensohler, A., Haneef, M. V., Imran, M., Warsi, A. B.,
695 Mandariya, A. K., Habib, G., and Pöhlker, M. L.: Significant contribution of fractal morphology to
696 aerosol light absorption in polluted environments dominated by black carbon (BC), npj Climate and
697 Atmospheric Science, 7, 87, 10.1038/s41612-024-00634-0, 2024.

698 Schloesser, H.: Use of a Multi-Wavelength Integrating Nephelometer to Determine Source Influences on
699 Particle Concentration Measurements. Atmospheric optics: aerosols, visibility and the radiativ
700 balance 2016, vol. 1: Atmospheric optics conference, 27-30 September 2016, Jackson Hole,
701 Wyoming, USA., 2016.

702 Schwarz, J. P., Katich, J. M., Lee, S. L., Thomson, D. S., and Watts, L. A.: "Invisible bias" in the single
703 particle soot photometer due to trigger deadtime, Aerosol Science and Technology, 56, 623-635,
704 10.1080/02786826.2022.2064265, 2022.

705 Seinfeld, J.: Atmospheric science - Black carbon and brown clouds, Nature Geoscience, 1, 15-16,
706 10.1038/ngeo.2007.62, 2008.

707 Stephens, M., Turner, N., and Sandberg, J.: Particle identification by laser-induced incandescence in a
708 solid-state laser cavity, Applied Optics, 42, 3726-3736, 10.1364/ao.42.003726, 2003.

709 Stier, P., Feichter, J., Kinne, S., Kloster, S., Vignati, E., Wilson, J., Ganzeveld, L., Tegen, I., Werner, M.,
710 Balkanski, Y., Schulz, M., Boucher, O., Minikin, A., and Petzold, A.: The aerosol-climate model
711 ECHAM5-HAM, Atmospheric Chemistry and Physics, 5, 1125-1156, 10.5194/acp-5-1125-2005,
712 2005.

713 Szopa, S., Naik, V., Adhikary, B., Artaxo, P., Berntsen, T., Collins, W. D., Fuzzi, S., Gallardo, L.,
714 Kiendler-Scharr, A., Klimont, Z., Liao, H., Unger, N., and Zanis, P.: Short-Lived Climate Forcers.
715 In Climate Change 2021: The Physical Science Basis. Contribution of Working Group I to the Sixth
716 Assessment Report of the Intergovernmental Panel on Climate Change (eds Masson-Delmotte, V.
717 et al.), IPCC, 2021.

718 Ueda, S., Nakayama, T., Taketani, F., Adachi, K., Matsuki, A., Iwamoto, Y., Sadanaga, Y., and Matsumi,
719 Y.: Light absorption and morphological properties of soot-containing aerosols observed at an East
720 Asian outflow site, Noto Peninsula, Japan, Atmospheric chemistry and physics, 16, 2525-2541,
721 10.5194/acp-16-2525-2016, 2016.

722 Wang, J., Wang, J., Cai, R., Liu, C., Jiang, J., Nie, W., Wang, J., Moteki, N., Zaveri, R. A., Huang, X.,
723 Ma, N., Chen, G., Wang, Z., Jin, Y., Cai, J., Zhang, Y., Chi, X., Holanda, B. A., Xing, J., Liu, T., Qi,
724 X., Wang, Q., Pöhlker, C., Su, H., Cheng, Y., Wang, S., Hao, J., Andreae, M. O., and Ding, A.:
725 Unified theoretical framework for black carbon mixing state allows greater accuracy of climate
726 effect estimation, Nature Communications, 14, 2703, 10.1038/s41467-023-38330-x, 2023.

727 Wang, T. T., Zhao, G., Tan, T. Y., Yu, Y., Tang, R. Z., Dong, H. B., Chen, S. Y., Li, X., Lu, K. D., Zeng,
728 L. M., Gao, Y. Q., Wang, H. L., Lou, S. R., Liu, D. T., Hu, M., Zhao, C. S., and Guo, S.: Effects of
729 biomass burning and photochemical oxidation on the black carbon mixing state and light absorption
730 in summer season, *Atmospheric Environment*, 248, 10.1016/j.atmosenv.2021.118230, 2021a.

731 Wang, Y., Pang, Y., Huang, J., Bi, L., Che, H., Zhang, X., and Li, W.: Constructing Shapes and Mixing
732 Structures of Black Carbon Particles With Applications to Optical Calculations, *Journal of*
733 *Geophysical Research: Atmospheres*, 126, 10.1029/2021jd034620, 2021b.

734 Wang, Y., Li, W., Huang, J., Liu, L., Pang, Y., He, C., Liu, F., Liu, D., Bi, L., Zhang, X., and Shi, Z.:
735 Nonlinear Enhancement of Radiative Absorption by Black Carbon in Response to Particle Mixing
736 Structure, *Geophysical Research Letters*, 48, 10.1029/2021gl096437, 2021c.

737 Weber, P., Petzold, A., Bischof, O. F., Fischer, B., Berg, M., Freedman, A., Onasch, T. B., and Bundke,
738 U.: Relative errors in derived multi-wavelength intensive aerosol optical properties using cavity
739 attenuated phase shift single-scattering albedo monitors, a nephelometer, and tricolour absorption
740 photometer measurements, *Atmospheric Measurement Techniques*, 15, 3279-3296, 10.5194/amt-
741 15-3279-2022, 2022.

742 Wu, Y., Cheng, T., and Zheng, L.: Light absorption of black carbon aerosols strongly influenced by
743 particle morphology distribution, *Environmental Research Letters*, 15, 94051, 10.1088/1748-
744 9326/aba2ff, 2020.

745 Zanatta, M., Gysel, N., Bukowiecki, T., Müller, E., and Weingartner: A European aerosol
746 phenomenology-5: Climatology of black carbon optical properties at 9 regional background sites
747 across Europe, *Atmospheric Environment*, 2016.

748 Zanatta, M., Bogert, P., Ginot, P., Gong, Y., Hoshyaripour, G. A., Hu, Y., Jiang, F., Laj, P., Li, Y., Linke,
749 C., Möhler, O., Saathoff, H., Schnaiter, M., Umo, N. S., Vogel, F., and Wagner, R.: AIDA Arctic
750 transport experiment – Part 1: Simulation of northward transport and aging effect on fundamental
751 black carbon properties, *Aerosol Research*, 3, 477-502, 10.5194/ar-3-477-2025, 2025.

752 Zeng, L., Tan, T., Zhao, G., Du, Z., Hu, S., Shang, D., and Hu, M.: Overestimation of black carbon light
753 absorption due to mixing state heterogeneity, *npj Climate and Atmospheric Science*, 7, 2,
754 10.1038/s41612-023-00535-8, 2024.

755 Zhai, J., Yang, X., Li, L., Bai, B., Liu, P., Huang, Y., Fu, T.-M., Zhu, L., Zeng, Z., Tao, S., Lu, X., Ye, X.,
756 Wang, X., Wang, L., and Chen, J.: Absorption Enhancement of Black Carbon Aerosols Constrained
757 by Mixing-State Heterogeneity, *Environmental Science & Technology*, 56, 1586-1593,
758 10.1021/acs.est.1c06180, 2022.

759 Zhang, F., Shen, J., Xu, D., Shen, J., Qin, Y., Shi, R., Wei, J., Xu, Z., Pei, X., Tang, Q., Chen, H., Xu, B.,
760 and Wang, Z.: Unveiling the key drivers and formation pathways for secondary organic aerosols in
761 an eastern China megacity, *Journal of Hazardous Materials*, 498, 10.1016/j.jhazmat.2025.139925,
762 2025a.

763 Zhang, J., Wang, Y., Teng, X., Liu, L., Xu, Y., Ren, L., Shi, Z., Zhang, Y., Jiang, J., Liu, D., Hu, M., Shao,
764 L., Chen, J., Martin, S. T., Zhang, X., and Li, W.: Liquid-liquid phase separation reduces radiative
765 absorption by aged black carbon aerosols, *Communications Earth & Environment*, 3, 128,
766 10.1038/s43247-022-00462-1, 2022.

767 Zhang, R. Y., Khalizov, A. F., Pagels, J., Zhang, D., Xue, H. X., and McMurry, P. H.: Variability in
768 morphology, hygroscopicity, and optical properties of soot aerosols during atmospheric processing,
769 *Proc. Natl. Acad. Sci. U. S. A.*, 105, 10291-10296, 10.1073/pnas.0804860105, 2008.

770 Zhang, Y., Zhang, Q., Cheng, Y., Su, H., Li, H., Li, M., Zhang, X., Ding, A., and He, K.: Amplification

771 of light absorption of black carbon associated with air pollution, *Atmospheric Chemistry and*
772 *Physics*, 18, 9879-9896, 10.5194/acp-18-9879-2018, 2018.

773 Zhang, Y., Zhang, Q., Cheng, Y., Su, H., Kecorius, S., Wang, Z., Wu, Z., Hu, M., Zhu, T., Wiedensohler,
774 A., and He, K.: Measuring the morphology and density of internally mixed black carbon with SP2
775 and VTDMA: new insight into the absorption enhancement of black carbon in the atmosphere,
776 *Atmospheric Measurement Techniques*, 9, 1833-1843, 10.5194/amt-9-1833-2016, 2016.

777 Zhang, Y. X., Zhang, Q., Yao, Z. L., and Li, H. Y.: Particle Size and Mixing State of Freshly Emitted
778 Black Carbon from Different Combustion Sources in China, *Environmental Science & Technology*,
779 54, 7766-7774, 10.1021/acs.est.9b07373, 2020.

780 Zhang, Z., Wang, J., Wang, J., Riemer, N., Liu, C., Jin, Y., Tian, Z., Cai, J., Cheng, Y., Chen, G., Wang,
781 B., Wang, S., and Ding, A.: Steady-state mixing state of black carbon aerosols from a particle-
782 resolved model, *Atmospheric Chemistry and Physics*, 25, 1869-1881, 10.5194/acp-25-1869-2025,
783 2025b.

784 Zhao, G., Shen, C., and Zhao, C.: Technical note: Mismeasurement of the core-shell structure of black
785 carbon-containing ambient aerosols by SP2 measurements, *Atmospheric Environment*, 243, 117885,
786 10.1016/j.atmosenv.2020.117885, 2020.

787